IOP Publishing J. Phys. Mater. **9** (2026) 025005 https://doi.org/10.1088/2515-7639/ae46e1

Journal of Physics: Materials

RECEIVED
18 September 2025

REVISED
18 January 2026

ACCEPTED FOR PUBLICATION
17 February 2026

PUBLISHED
26 February 2026

PAPER

Hybrid films of Co–C_{60} preparation and changes induced by external stimuli

Giovanni Ceccio[1,*], **Jiri Vacik**[1], **Yuto Kondo**[2], **Kazumasa Takahashi**[2], **Romana Miksova**[1], **Eva Stepanovska**[1,3], **Josef Novak**[1,3], **Petr Malinsky**[1,3], **Barbara Fazio**[4], **Catia Cannilla**[5], **Alena Michalcova**[6] **and Sebastiano Vasi**[7,8,*]

[1] Department of Neutron and Ion Methods, Nuclear Physics Institute of Czech Academy of Science, Řež 292, Husinec, 25068, Czech Republic
[2] Department of Electrical Engineering, Nagaoka University of Technology, 1603-1 Kamitomioka, Nagaoka, Niigata 940-2188, Japan
[3] Department of Physics, Faculty of Science, J. E. Purkyne University in Ústí nad Labem, Pasteurova 3632/15, 400 96 Ústí nad Labem, Czech Republic
[4] IMM-CNR sede di Messina, Viale Ferdinando Stagno d'Alcontres, 31, 98166 Messina, Italy
[5] CNR-ITAE, Istituto di Tecnologie Avanzate per l'Energia, Via S. Lucia Sopra Contesse 5, 98126 Messina, Italy
[6] Department of Metals and Corrosion Engineering, University of Chemistry and Technology in Prague, Technicka 5, Prague, 166 28, Czech Republic
[7] Department of Mathematics and Computer Sciences, University of Messina, Physical Sciences and Earth Sciences, Viale F. Stagno d'Alcontres 31, 98166 Messina, Italy
[8] OPENFIS S.R.L. - SPIN OFF ACCADEMICO, LABORATORIO A2AT3, University of Messina, Viale F. Stagno D'Alcontres 31, 98166, Messina, Italy
[*] Authors to whom any correspondence should be addressed.

E-mail: ceccio@ujf.cas.cz and vasis@unime.it

Keywords: cobalt, fullerene, thin film, annealing, ion irradiation

Supplementary material for this article is available online

Abstract

In this work, we report on the study on organic-metal hybrid systems, in particular Co–C_{60} fullerene thin films. This study mainly focused on the investigation of the morphological and structural evolution of the film surface after various external stimuli designed to provide energy to the system. For film growth, we adopted an innovative approach, combining ion beam sputtering of a pure metal target with thermal evaporation of C_{60} in a co deposition setup. The films underwent a series of treatments to induce modifications. Laser and ion irradiations were performed using a pulsed laser, a continuous Ar beam, and a pulsed C beam. In addition, thermal annealing in vacuum was performed to examine the long-term effects of temperature. The composition of deposited film was investigated using ion beam analysis, the morphology and the structure, and the effects of treatments on the films were studied using scanning electron microscope and transmission electron microscopies and Raman spectroscopy. Changes in electrical resistance were also measured to explore potential applications of these films after treatment.

1. Introduction

Recent advances in nanoscience, particularly in nanoarchitectures, highlight metal-organic hybrid nanostructures as an increasingly relevant research topic, yielding intriguing results in electronics and proposing advanced applications, such as catalysis and electrochemistry, energy storage and conversion, gas sensing and spintronics [1–16]. The study of C_{60} fullerene in such hybrid systems is often taken into consideration due to the unique properties of C_{60} molecules, such as the exciting atomic structure, the intriguing coupling with metals, the tiny hyperfine interactions, the greater structural stability and the relative low cost. These features collectively increase the interest in such materials [17–22]. Among various C_{60}-based hybrid systems, self-assembled nanostructured materials are particularly notable for their tunability, offering precise control over the nanostructure during growth or post-production to tailor their electrical properties. The discovery of higher conductivity and superconductivity in alkali metal fullerides has also been a strong motivation for the implementation of transition metal (TM)-fullerene related research [20, 23–25]. Attempts to combine TMs and C_{60} via co-deposition to access TM-fullerides have usually revealed pronounced metal clustering (due to the high cohesive energy of metals) with separation from C_{60} phase, which hinders homogeneous mixing but also enables additional functional behavior of such nanostructures [25, 26]. An example is given by structures based on the coexistence of Co and C_{60}, in both homogeneous compounds and heterogeneous films, which have a great impact in spintronics due to the catalytic and magnetic properties of Co [17, 27–31]. Furthermore, such hybrid systems have gained interest for potential applications in lithium-ion batteries [32], where structural stability, conductivity, and controlled phase evolution are critical for improving performance and longevity. Besides their interesting properties, however, integrated hybrid systems are considered thermodynamically and structurally unstable (mainly due to the high internal stress resulting from the mixing of mostly immiscible phases and the vulnerability of C_{60} molecular cages due to their easy photo-oxidation, polymerization or fragmentation in an environment exhibiting strong catalytic properties) [33–35]. This makes their possible applications more challenging. The use of various disruptive agents (such as thermal annealing, ion irradiation, laser illumination, chemical reagents, etc) can significantly influence thermodynamically unstable systems, inducing their structural changes at the nanoscopic and macroscopic scales as the system moves toward a state of minimum energy. This approach not only enables control over material properties for specific applications, but also serves as a model for studying the long-term evolution of these hybrid systems under extreme conditions, which is highly relevant for their potential integration into devices designed for harsh environments (e.g. space applications, high-radiation areas, and extreme temperature conditions). While numerous studies have investigated the growth, structure, and intrinsic properties of metal-C_{60} hybrid systems, most reported works focus on as-deposited films or on single modification routes, often produced under different deposition conditions or with varying compositions [25, 27, 36]. As a result, a direct and systematic comparison of how different external stimuli influence the same Co–C_{60} system remains limited [20]. The ability to intentionally modify the system provides the advantage of preventing unwanted changes due to system aging or adverse environmental conditions during the lifetime of a possible device based on such systems. Our previous systematic works [37–39] have focused on study the physical properties of systems realized using different ratios of constituents within thin films. In contrast to these previous studies, the present work does not aim to explore new compositions or mixing ratios, but rather to isolate the effects of different post-deposition energy inputs applied to films fabricated under strictly identical growth conditions. This post-treatment-centered approach allows us to disentangle how distinct excitation pathways drive structural reorganization and functional property changes in the same hybrid system. The prepared samples have been exposed to vacuum annealing, pulsed laser irradiation, and ion irradiation (continuous beam and pulsed beam). The analyses performed show that the hybrid systems evolved in different ways, exhibiting diversification in their nanostructures and macrostructures depending on the external perturbation applied.

2. Materials and methods

We have produced a set of Co–C_{60} mixture films by co-deposition of Co and C_{60} on Si(110) substrates in high vacuum (base vacuum, 2E-6 mbar). The growth of the Co film was performed by the ion beam sputtering technique realized by using a low energy ion facility (LEIF) [32, 40], operating with a beam of Ar^+ ions accelerated at 20 keV and focused on a Co target (2 inch × 0.125 inch, 99.99% purity, Kurt J. Lesker) mounted on a suitable target holder and inclined at 45° with respect to the beam. The target faces the substrates mounted at a distance of 100 mm, under an angle of 30°. Just below the substrate holder, at the distance of 10 mm, a lab made evaporator that acts as a source of C_{60} (99.9% purity, Nanografi) is present, in order to perform simultaneous deposition of Co and C_{60} (see sketch if figure 1). The evaporator, equipped with digital temperature control and a thermocouple inserted directly into the crucible, was maintained at a temperature of 450 °C for the entire duration of the deposition. During the beam calibration and heat up procedure of the crucible, a shutter is present to avoid unwanted depositions on the substrates. For transmission electron microscopy (TEM) analytical purpose, samples were deposited on 300 mesh Cu TEM grids with holey carbon films (TedPella, Inc.).

All films were deposited together in order to guarantee the same experimental parameters and the same film on all substrates. ion beam analysis experiments were performed at the Tandetron MC 4130 tandem accelerator located at Nuclear Physics Institute (NPI). Rutherford backscattering spectrometry (RBS) and elastic recoil detection analysis (ERDA) were used for the analysis. To identify heavier

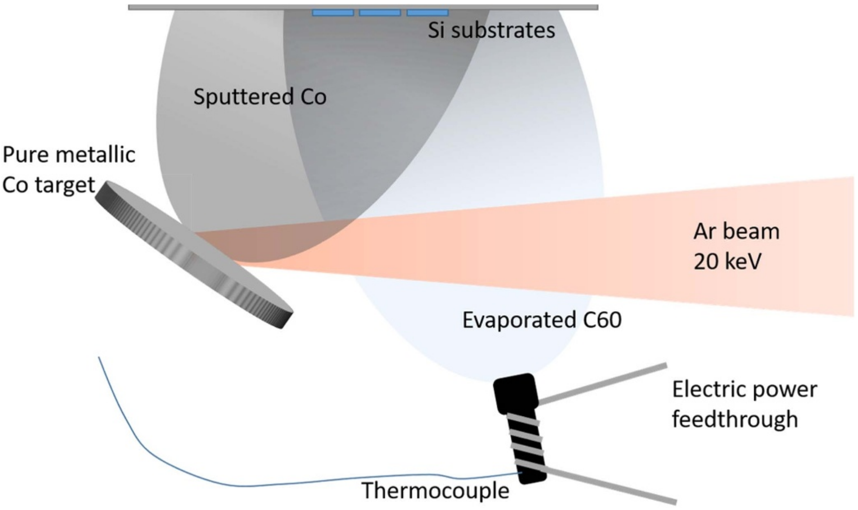

Figure 1. Deposition scheme with IBS setup and thermal evaporator.

elements, He$^+$ ions with an energy of 2 MeV were used, while for the carbon detection H$^+$ ions at 1.735 MeV were chosen, hitting the films with an incident angle of 7°). The backscattered ions were detected using an ORTEC ULTRA-series detector, which features a 50 mm^2 active area and a 300 μm thick depletion layer. The detector was positioned at a backscattering angle of 170° out of the plane, in accordance with Cornell geometry. In the ERDA measurement, He$^+$ ions with an energy of 2.5 MeV were utilized to identify H, and the detector was placed at a backscattering angle of 30° in the plane, following the IBM geometry. The recoiled particles were detected by a Canberra PIPS detector preceded by a 12 μm thick Mylar foil. Data obtained by ion beam analysis were processed using the SIMNRA code [41]. The irradiation of the samples by means of a continuous beam of Ar$^+$ was carried out using the LEIF (NPI) system, positioning the samples orthogonal to the beam in place of the sputtering target. For irradiation, an energy of 20 keV and a current of 500 μA were used up to a total fluence of 1×10^{-15} Ar cm^{-2}. Another sample set was irradiated at the same fluence and energy using a pulsed C$^+$ beam. A laser ion source (Nagaoka University) was used to produce a pulsed C beam. The used laser source was a Quantel Brilliant operating at 10 Hz repetition rate, 6 ns pulse duration, 532 nm wavelength and laser energy of 130 mJ . The laser pulse was focused (in vacuum) on the surface of a C target held at a voltage of 20 kV and facing the grounded samples. To reach the same fluence used for the Ar beam, a total of 12 000 pulses were needed for each sample. An additional set of samples was exposed directly to the laser source, to induce changes on the surface. The laser irradiations occurred in air, without laser focusing and at an energy of 5 mJ per pulse. Each sample was irradiated with 1000 pulses. The annealing was performed using a special vacuum chamber with a heating system inside. The annealing was performed in a vacuum level of 1×10^{-5} mbar and for a duration of 5 h (without considering the cooling time) at temperature of 300 °C. The samples, pristine and modified, were investigated for morphological evolution by scanning electron microscopy (SEM) Hitachi-SU8230. Additional morphological study with elemental mapping of the materials was carried out using the Thermo Scientific Helios™ 5 UC dual beam SEM-field emission gun (FEG)-ultra high resolution (UHR) equipped with different detector Everhart–Thornley detector, through-the-Lens and scanning TEM. The elemental analysis and mapping were carried out by using the energy dispersive analysis system (EDX). Measurements were carried out with an operating voltage between 10 and 30 kV, without pretreatment of the samples. The TEM analysis of microstructure was performed by use of Jeol 2200 FS (Jeol,Tokio, Japan) FEG equipped with an Oxford Instruments EDS analyzer, instrument operating at a 200 kV accelerating voltage with a point resolution of 2.4 Å. The micrographs have been carried out using a TVIPS camera and EM-Menu software.

Raman spectroscopy measurements were also performed, using a LabRam HR-EVO Horiba operating at 532 nm, 50X LWD with power 0.8 mW per μm^2 and CCD Syncerity Horiba and NRS 7200 microRaman spectrometer with 532 nm wavelength and applied power 6.5 mW. In particular, the microRaman spectrometer was used for the evaluation of the as-deposited and modified films, on the other hand the Raman spectrometer was used for the fullerene characterization. Changes in electrical resistivity of the pristine and modified samples, were investigated using 2182A Nanovoltmeter and 6221 DC current source Keithley on the surface of sample, in a galvanostatic setup. The measurements were performed using the standard two-point method in air and room temperature. While the two-point method includes contact and lead resistances, all measurements were performed under identical conditions, allowing reliable comparison of relative resistance changes induced by different treatments.

3. Results

The chemical composition of the produced films was investigated after deposition using RBS and ERDA techniques. These scattering techniques are used for compositional thin film analysis, based on stopping power and inelastic energy loss during ion-solid interactions and the kinematically recoil. In our case, RBS is particularly suitable for the detection of heavy Co atoms (because light C atoms are hidden by Silicon signal), meanwhile the ERDA is used for H detection. Experimental results relative to 2 MeV He^+ are shown in figure 2 with simulated fit. Note that the spectra were normalized to the substrate. Carbon measurements were performed using 1.735 MeV H^+ ions and different incident ions angle (0 degrees were used for measurement with He^+ analysis and 7° for the H^+). The relative spectra are illustrated in figure S1 of the supplementary information (SI). Table 1 includes all the elemental concentrations' values of the data acquired by performing RBS and ERDA analyses on Co and Co–C_{60} films. RBS measurements confirm that CoC_{60} hybrid films have been successfully fabricated.

Oxygen and carbon contaminations as well as hydrogen content are detected in the produced films. The sample with C_{60} show almost a ratio 3:2 between Co and C atoms. It should be noted that the pure Co film was prepared and analyzed exclusively as a compositional and structural reference for ion beam analysis. The electrical, morphological, and post-treatment comparisons discussed in this work are performed only among Co–C_{60} hybrid films, which share the same deposition conditions and comparable thickness. Therefore, the difference in areal density between pure Co and Co–C_{60} films does not introduce bias in the comparative interpretation of the hybrid film properties.

Presence of oxygen in the deposited films can be explained as oxidation of the Co NPs (possibly formed in the film nanostructure) during the air exposure of the samples.

The quantity of oxygen is independent of the presence of C_{60} or the ratio between Co and C_{60}. This may suggest that the detected oxygen is bounded chemically to the cobalt, forming more realistic composition $Co_xO_yC_{60}$. By coming into contact with the Co clusters, the O_2 molecules react with the Co surface causing O_2 dissociation and formation of the Co_xO_y [42]. By considering that the presence of C atoms in pure Co film (due to vacuum contamination by partial sputter of holder and shutter probably) and Co–C_{60} film are 14% and 33%, respectively, we can confirm that the C_{60} is almost the 20% of the film, so the majority of the film consists of Co atoms. As illustrated in figure S2 of SI, the RBS analysis allows us to also establish that the distributions of Co and C, as well as the other elements, within the thickness of the samples are constant. Furthermore, thanks to the ERDA results, the presence of about 10% of H atoms was measured and confirmed as shown later by Raman analysis.

Figure 3 reports the SEM images for the as prepared samples and figure 4 shows elemental mapping of selected particles obtained using EDX analysis. In the SEM micrograph of pristine sample, smooth surface and uniform particles distribution are recognized, indicating homogeneous mixture with few visible micron sized particles. EDX analyses reported in figure 4 were performed on a selected particle to understand its composition. It was found a deficiency of Co inside the particle with a Co-enriched ring around it, and uniform distribution anywhere else. In order to observe the formed nanostructures in the hybrid CoC_{60} films, we performed detailed TEM analyses on the as deposited film. So, following the procedure reported in the 'materials and methods' section, we deposited the sample on Cu holey carbon grid to analyze it for structural information. Figure 5 shows the TEM image obtained from the $CoOC_{60}$ film. The sample has composite nanostructure consisting of small Co nanoparticles distributed uniformly. Samples subject to modification were analyzed from morphological point of view as the pristine one. The SEM images from the modified samples are reported in figure 6 taken at a magnification of 2.5kx. For each of these samples was performed as well elemental mapping with EDX analysis on selected particles.

All treatments applied to the films to alter their properties and morphologies resulted in the development of numerous structures on the surface. One of the possible reasons behind these phenomena is the stress accumulated on the surface (and immediately under the surface) during the deposition, due to the immiscibility of the materials. This stress is released almost instantaneously with the treatments, creating separation of the phases. The energy in excess, provided by the treatment is used for the growth of structures around the nucleation point. Depending on the available energy, more or less organized structures can form.

From the large area SEM, the sample that was subjected to annealing (figure 6(a)) presents structures tending to the circular shape, with a strong nucleation of C_{60} above the Co (or viceversa). Some

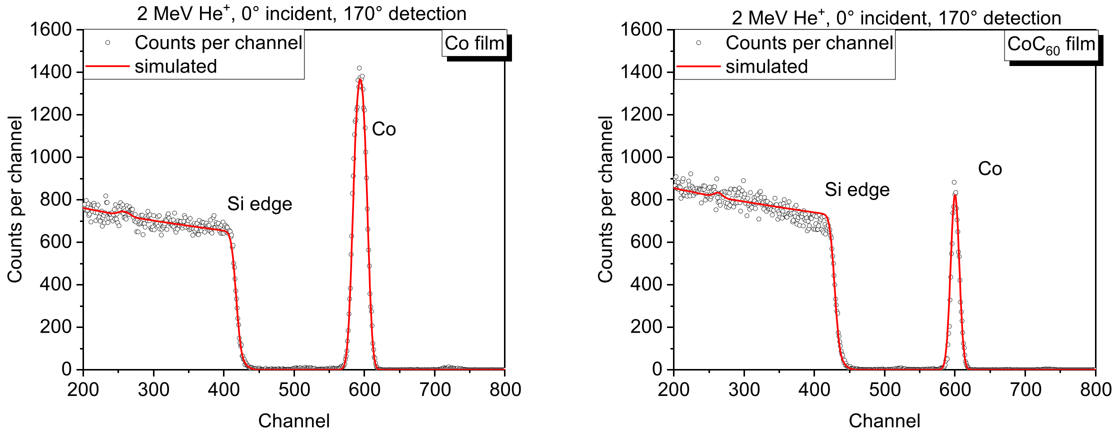

Figure 2. RBS results on pure Co and Co–C_{60} samples obtained with 2 MeV He^+. Black dots are experimental data and the red line represents the fit obtained from SIMNRA simulation.

Table 1. Elemental composition of samples calculated by RBS-ERDA analysis using both 2 MeV He^+ beam and 1.735 MeV H^+.

Sample	Co (at. %)	C (at. %)	O (at. %)	H (at. %)	Thickness (10^{15} at cm^{-2})
Co film	70	14	5	11	480
Co–C_{60} film	50	33	3	14	245

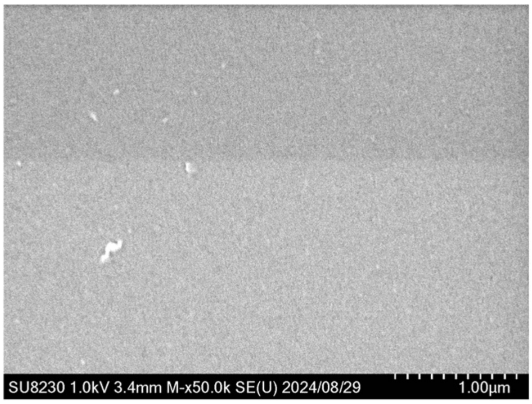

Figure 3. SEM pictures taken at 50kX magnification of as deposited sample.

structures show a main nucleation surrounded by a huge number of smaller nucleations (see figureS3 of SI for additional pictures). The sample exposed to Ar^+ beam irradiation (figure 6(b)) displays a great number of very small separation spots, non-organized and spread randomly on the surface (see figure S4 of SI for additional pictures). The C^+ irradiation (figure 6(c)) did not produce a particular separation on this films surface at least visible, but possible compositional changes in the C phase (see figure S5 of SI for additional pictures). The laser irradiation showed in figure 6(d) produced large spots with C nucleation, but also microstructures with resemblance of long crystal structures (see figure S6 of SI for additional pictures). The EDX mapping shows that the agglomerations of particles are formed by both constituents, with little more content of C in the center. Compared with the pristine sample there is the elemental distributions are more homogeneous, due to the release of existing stress. Additional EDX mapping are shown in SI figure S7–10.

A detailed Raman analysis of the pristine films of pure and hybrid materials was performed. Figure 7 shows the Raman spectra of the C_{60} film deposited on the silicon substrate, compared to the vibrational fingerprint of pure C_{60} powder used as a precursor in film preparation, obtained by excitement with a 532 nm laser wavelength. The Raman spectrum of the C_{60} powder (black line) displays several Raman contributions between 1000 and 2000 cm^{-1}, closely matching values found in the literature [43, 44]. Notably the Raman-active modes of H_g symmetry are found at ~1100 cm^{-1} ($H_g(5)$), ~1250 cm^{-1}

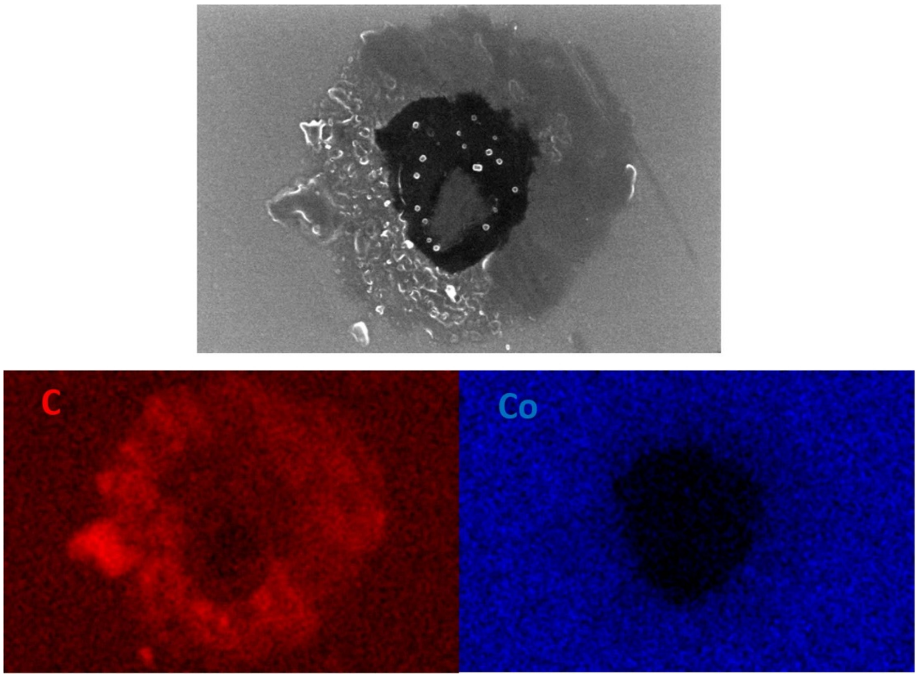

Figure 4. Elemental mapping of particle on the as deposited sample.

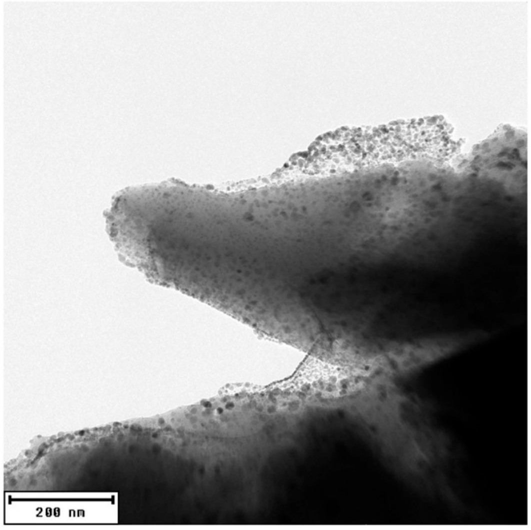

Figure 5. TEM micrograph of as prepared sample.

($H_g(6)$), ~1424 cm^{-1}($H_g(7)$), and 1581 cm^{-1}($H_g(8)$). In this Raman shift region, the peak at 1462 cm^{-1} is assigned to the $A_g(2)$ mode, known as 'pentagonal pinch' since caused by the contraction of the pentagonal rings and the expansion of the hexagonal rings of carbon atoms. These peaks overlay the broader bands observed in the spectral ranges of 1330–1360 cm^{-1} and 1560–1600 cm^{-1}, corresponding to the D and G bands, respectively, which are characteristic of all carbon-based materials under visible-range excitation [45]. Notably, laser heating during Raman measurements can facilitate the formation of additional carbon phases.

The complete spectrum of C_{60} powder, which includes the remaining four low-frequency H_g symmetry modes and the purely radial $A_g(1)$ mode at 496 cm^{-1}, is shown in figure S11 of the SI. The Raman spectrum of C_{60} film (red line in figure 7) shows a distinctive peak at 1450 cm^{-1} (highlighted by asterisk), which attests a photo-transformed state of C_{60} and the presence of polymer chains that, in the case of film, easily form during laser irradiation in Raman measurements [43]. Furthermore, the $A_g(2)$

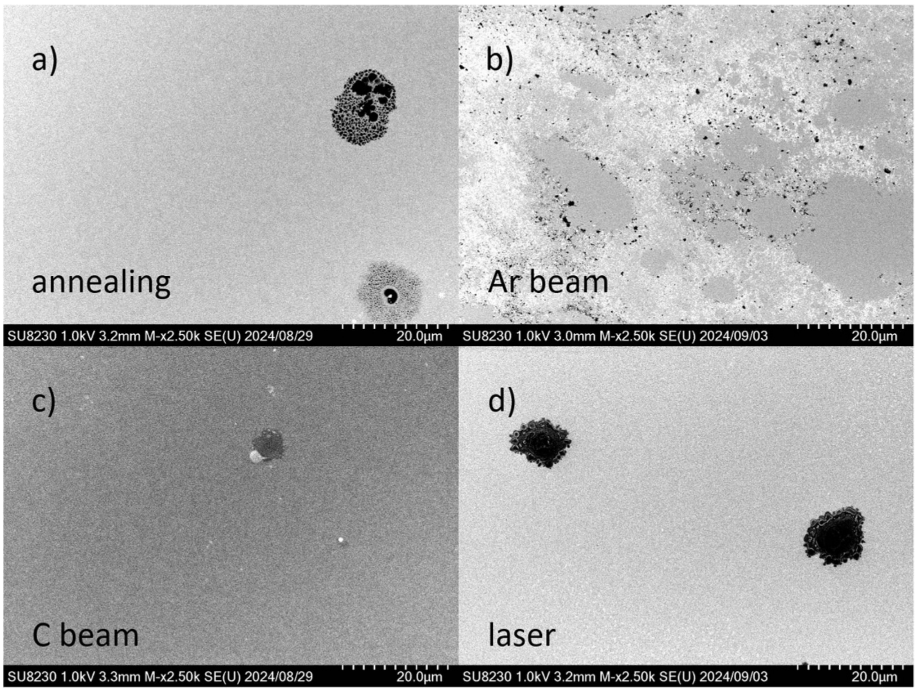

Figure 6. SEM pictures taken at 2.5kX magnification modified samples.

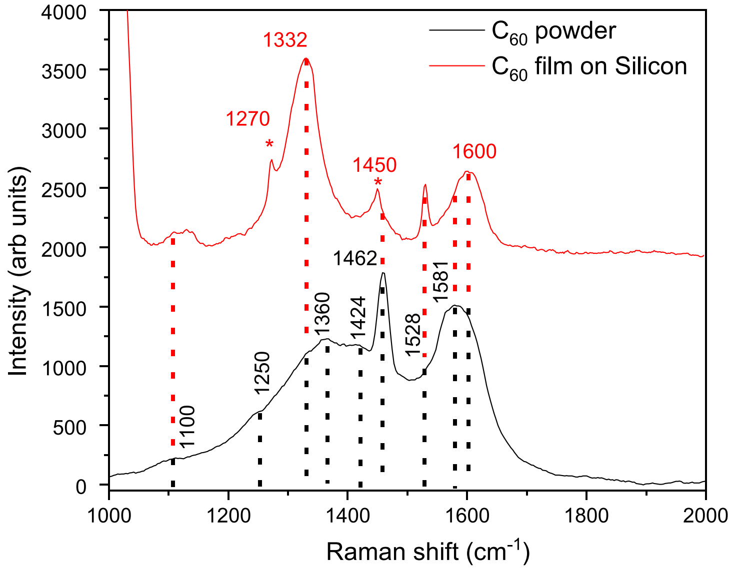

Figure 7. Raman spectrum of C_{60} powder (black line) and C_{60} film deposited onto silicon substrate (red line). Peaks exclusive to the C_{60} film spectrum are marked with asterisks, while the dotted lines (black and red) highlight peaks common to both C_{60} powder and film.

peak at 1462 cm^{-1}, characteristic of the C_{60} powder, almost disappears in the fullerene film as it is overshadowed by the tail of the prominent peak at 1450 cm^{-1}. It is worthy to note the presence of the wide D band mainly peaked at 1332 cm^{-1}, typical of diamond-like carbon materials. The peak at 1270 cm^{-1} (highlighted by asterisk) is ascribed to a combination of antisymmetric C–C interring stretching mode and antisymmetric bending mode of C–H groups that form on fullerene surface [46]. The prominent and sharp peak tail that diminishes at 1065 cm^{-1} corresponds to the second-order Raman peak of the Si substrate. Figure 8 displays the Raman spectra of hybrid Co–C_{60} films, both pristine and post-treatment, within the 800–1800 cm^{-1} spectral range. Notably, the characteristic $A_g(2)$ peak at 1462 cm^{-1} is significantly broadened and overlaps with the D and G bands (at 1360 and 1562 cm^{-1}, respectively),

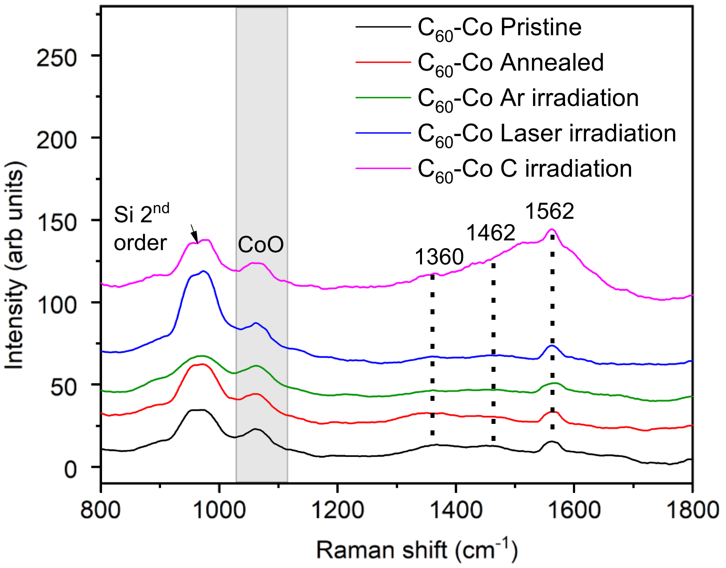

Figure 8. Raman spectra of hybrid Co–C_{60} films, as deposited (black line) onto silicon substrate and post-treatments: Co–C_{60} film annealed (red line), Co–C_{60} film Ar irradiated (green line), Co–C_{60} film laser irradiated (blue line), and Co–C_{60} film C irradiated (magenta line). The spectra are stacked in intensity for a better visualization.

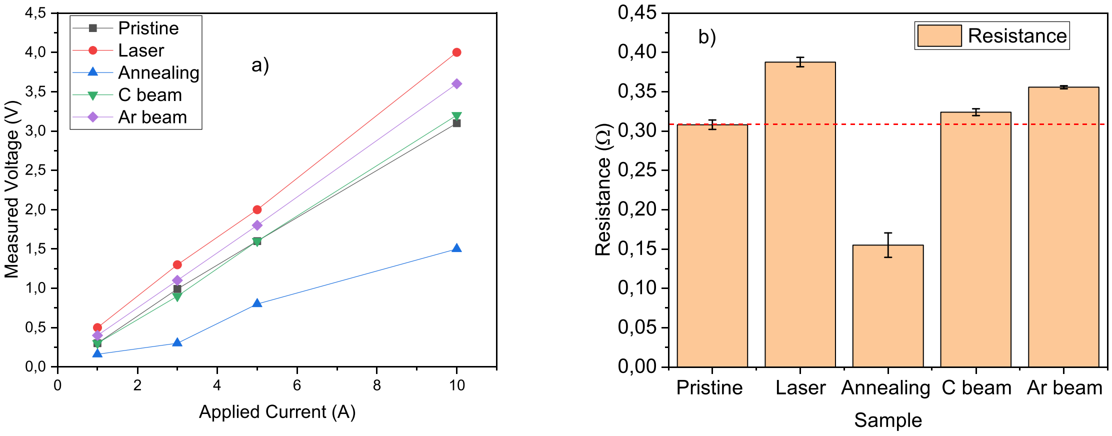

Figure 9. Results of galvanostatic measurement (a) and calculated electrical resistance (b), measured using 2-points method.

which are typical features of carbon materials. When the Co–C_{60} is irradiated by carbon beam, a pronounced broad band appears beneath this peak, which is attributed to the formation of amorphous carbon. Furthermore, all spectra exhibit a broad band in the spectral range between 1030 and 1100 cm^{-1} (gray rectangle in figure 8), attributed to the second-order two-phonon Raman scattering of the CoO phase [47]. This spectral feature indicates cobalt oxidation induced in defective sites of cobalt during the co-deposition of hybrid films. Under laser heating during Raman measurements, the CoO phase readily transforms into the Co_3O_4 phase [48].

The results concerning the electrical resistance measurements performed on the films are shown in figure 9. Figure 9(a) shows the galvanostatic measurements performed on the samples surface, using the setup described in 'material and methods' section. The voltage measured with a nanovoltmeter between the electrodes that applied stabilized current to the films were recorded for several applied current values that ranged from 1 A to 10 A. Figure 9(b) illustrates the resistance calculated by linear regression of the data in figure 9(a). If we consider the pristine Co–C_{60} film, it shows a resistance of 0.308 Ω. It is a valid assumption considering this value as the reference for all the deposited films when the samples were all produced together during the same deposition. In this way, the measured variations in the resistance values are due only to the treatments to which they were exposed. Irradiation with a laser beam as well as bombardment with charged particles increased the resistance of the samples. In particular, laser irradiation leads to the highest resistance observed. An interesting result is instead the one referring to the

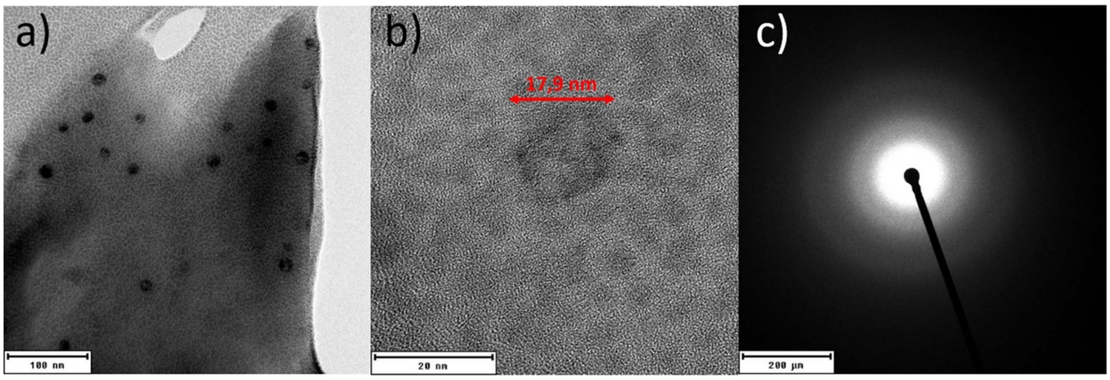

Figure 10. TEM micrograph of annealed sample, magnification of fullerene NPs and SAED of area in picture.

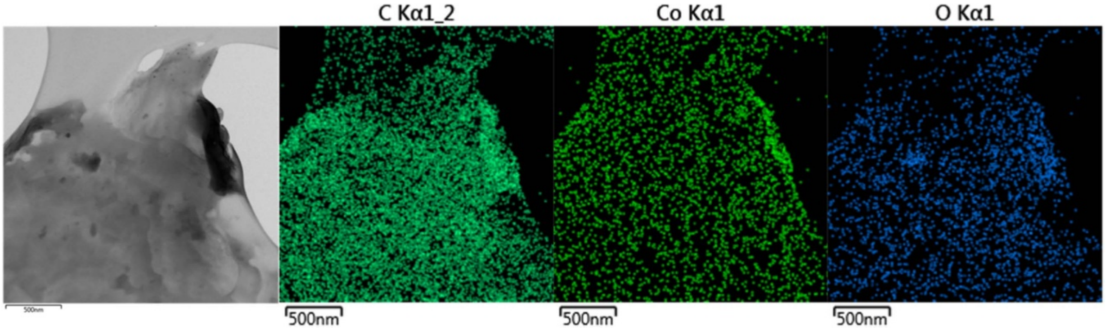

Figure 11. Elemental mapping of area shown in figure 10.

sample subjected to annealing, for which the resistance value is 0.155 Ω, almost half of the thin film in the pristine state. Probably, the annealing process produces large enucleations of C_{60}, separating the metal from the fullerene more clearly and the reduction in resistance observed after annealing is attributed to phase segregation and morphological reorganization, which likely promotes the formation of percolative Co-rich conduction pathways, even in the presence of partial cobalt oxidation.

In order to investigate the origin of these particular electrical properties of the annealed samples, additional structural analyses were performed with TEM and the selected area electron diffraction (SAED) method on the grid sample. Figure 10(a) shows the morphology of selected area of modified film. It is possible to see agglomerations of self-assembled C_{60} nanoparticles of the size of 17.9 nm (figure 10(b)). Instead, the SAED analysis allows us to measure the lattice parameters, crystal structure, and extent of crystallinity of nanoparticles from the diffraction technique, in which the sample is targeted with a parallel beam of high energy electrons. In particular, figure 10(c) illustrates that the film is in an amorphous state as expected. Finally, this area of the annealed grid sample was selected to perform elemental mapping also with the aim of understanding the elemental distribution of the elements (figure 11). As shown by the oxygen mapping, cobalt effectively becomes oxidized, so the reduced electrical resistance has to be ascribable to a self-agglomeration of C_{60} fullerene. Unfortunately, the carbon distribution is affected by the holey C film on which it is deposited.

4. Discussion

The systematic study performed in this work is focused on the preparation of Co–C_{60} hybrid films under identical growth conditions and on their controlled modification through multiple external stimuli, enabling a direct comparison of distinct post-treatment pathways and their effects on nanostructure and functional properties. Well established ion beam analytical techniques, such as RBS and ERDA, have been used in the study to evaluate the film's original composition and thickness. 'As deposited' and modified samples revealed several important morphological and structure evolutions based on the applied external stimuli.

During the self-assembly of fullerene nanoparticles in a nonequilibrium solid-solution, C_{60} molecules form a nanoparticle, finding the most advantageous combination of interactions between molecules with minimal free energy. Considering the efforts usually required to prepare the nanoparticle by pulverization, the possibility to obtain nanosized C_{60} by dry physical method (in our case thermal evaporation) is truly an innovative result, considering that self-aggregation process of C_{60} particles is purely physical, and is not associated with visible changing in phase crystal structure. Interesting physical and structural properties were observed in the metal-C_{60} phase without and with separation induced by external perturbations. SEM analyses performed on treated samples showed strong separations of the immiscible phases. The magnitude of such separations was different for each applied perturbation, as well as for the final shapes of formed structures. The nucleation produced by some treatments (e.g. the annealing process) produced a quasi-perfect circular germination of the material surrounded by smaller separation areas. These strong separations sometimes occur with neither the growth of carbon structures above the film nor with the formation of cobalt structures above the film. The study conducted using Raman spectroscopy allowed for the identification of the characteristic C_{60} peak in the deposited film without Co, confirming the presence of the hollow structure of the fullerene. When combined with Co, there was a broadening of the characteristic $A_g(2)$ peak, with an overlapping of D and G bands. In particular, it was observed that after carbon irradiation, a pronounced broad band appears beneath this peak due to the strong amorphization of carbon. The band attributed to the oxides of cobalt are also detected revealing a transformation of CoO in Co_3O_4 phase, as confirmed by Rivas-Murias and Salgueiriño in their previous work [48]. Despite the presence of cobalt oxides, electrical resistance measurements revealed a non-monotonic response to the applied treatments. Ion and laser irradiation resulted in an increase in resistance, consistent with enhanced disorder, amorphization, and oxidation effects. In contrast, thermal annealing led to a pronounced reduction in the measured resistance in comparison to the pristine film. This behavior cannot be attributed to simple increase of Co amount, as oxidation of cobalt is clearly evidenced by Raman spectroscopy and elemental mapping. Instead, the reduced resistance observed after annealing is to be attributed to morphology-driven reorganization and phase segregation within the hybrid film. TEM analysis of the annealed samples reveals the formation of self-assembled C_{60} nanoparticles, indicating substantial molecular rearrangement and separation of the fullerene- and cobalt-rich regions. In such heterogeneous systems, cobalt is likely present in a mixed state comprising oxidized surface or interfacial regions surrounding Co-rich cores. In this case, electrical transport is governed by formation conduction pathways, where the macroscopic resistance is dominated by the connectivity of the most conductive regions rather than by the average phase composition.

Therefore, even in the presence of partial cobalt oxidation and intrinsically low fullerene conductivity, phase segregation induced by annealing can promote the formation of effective Co-rich conduction paths, resulting in a lower measured resistance. Overall, this study provides a comparative framework for understanding how different energy-delivery mechanisms affect Co–C_{60} hybrid systems. The post-treatment-focused approach presented here offers a valuable strategy for tailoring the functional properties of metal-organic hybrid films and can be extended to other immiscible composite systems relevant to electronics, spintronics, and energy-related applications.

Data availability statement

The data that support the findings of this study are openly available at the following URL/DOI: https://zenodo.org/uploads/18 230 442 [49].

Supporting Data: Co-C60 available at https://doi.org/10.1088/2515-7639/ae46e1/data1.

Funding

The authors acknowledge the financial support from the MEYS CR (Project OP JAK FerrMion, No. CZ.02.01.01/00/22_008/0004591. The authors acknowledged also the support of Czech Academy of Science Mobility Plus Project, Grant no. JSPS-24-12 and JSPS Bilateral Program Number JPJSBP120242501. Measurements were carried out at the CANAM infrastructure of the NPI CAS Rez under project LM 2015 056. B F acknowledges the Italian Project PNRR'I-PHOQS—Integrated Infrastructure Initiative in Photonic and Quantum Sciences, CUP B53C22001750006.'. Part of this research was conducted within the activities of the RTD-A contract of S Vasi co-funded by PON 'Ricerca e Innovazione' 2014-2020 (PON R&I FSE-REACT EU), Azione IV.6 'Contratti di ricerca su tematiche Green'. C C acknowledges the financial support by the European Union—NextGeneration EU PNRR IR0000020 ECCSELLENT through NRRP—M4C2, Inv. 3.1'Development of ECCSEL-R I Italian facilities: user access, services and long-term sustainability'

Author contributions

Giovanni Ceccio 0000-0001-7959-8815
Conceptualization (lead), Data curation (equal), Funding acquisition (lead), Investigation (equal), Methodology (equal), Resources (equal), Writing – original draft (equal)

Jiri Vacik 0000-0002-1875-4914
Conceptualization (equal), Resources (equal), Validation (equal), Visualization (equal)

Yuto Kondo 0009-0001-0382-5230
Formal analysis (equal), Investigation (equal)

Kazumasa Takahashi 0000-0001-7872-0225
Funding acquisition (equal), Investigation (equal), Methodology (equal), Project administration (equal)

Romana Miksova 0000-0002-8887-601X
Data curation (equal), Formal analysis (equal), Methodology (equal)

Eva Stepanovska 0000-0003-1973-6539
Data curation (equal), Methodology (equal)

Josef Novak 0000-0002-1231-4619
Formal analysis (equal), Investigation (equal)

Petr Malinsky 0000-0002-4236-1192
Investigation (equal), Methodology (equal)

Barbara Fazio 0000-0002-1947-1123
Data curation (equal), Formal analysis (equal), Investigation (equal)

Catia Cannilla 0000-0001-6773-3784
Formal analysis (equal), Investigation (equal)

Alena Michalcova 0000-0002-1225-5380
Formal analysis (equal), Investigation (equal)

Sebastiano Vasi 0000-0003-0480-3321
Data curation (equal), Formal analysis (equal), Investigation (equal), Validation (equal), Writing – original draft (equal)

References

[1] Scheele M, Brütting W and Schreiber F 2015 Coupled organic-inorganic nanostructures (COIN) *Phys. Chem. Chem. Phys.* **17** 97–111

[2] Goiri E, Borghetti P, El Sayed A, Ortega J E and de Oteyza D G 2015 Multi component organic layers on metal substrates *Adv. Mater.* **28** 1340–68

[3] Cui Y, Bin Li, Huajun H, Zhou W, Chen B and Qian G 2016 Metal-Organic frameworks as platforms for functional materials *Acc. Chem. Res.* **49** 483–93

[4] Devkota J, Geng R, Subedi R C and Nguyen T D 2016 Organic spin valves: a review *Adv. Funct. Mater.* **26** 3881–98

[5] Otero R, Vázquez de Parga A L and Gallego J M 2017 Electronic, structural and chemical effects of charge-transfer at organic/inorganic interfaces *Surf. Sci. Rep.* **72** 105–45

[6] Sosa J D, Bennett T F, Nelms K J, Liu B M, Tovar R C and Liu Y 2018 Metal-organic framework hybrid materials and their applications *Crystals* **8** 325

[7] Song X *et al* 2019 2D semiconducting metal-organic framework thin films for organic spin valves *Angew. Chem. Int. Ed.* **59** 1118–23

[8] Socol M, Preda N, Costas A, Borca B, Popescu-Pelin G, Mihailescu A, Socol G and Stanculescu A 2020 Thin films based on cobalt phthalocyanine:C_60 fullerene:ZnO hybrid nanocomposite obtained by laser evaporation *Nanomaterials* **10** 468

[9] Shao Z, Chen J, Gao K, Xie Q, Xue X, Xue Li, Hou H and Liwei Mi 2023 A high-spintronic helix metal-organic chain as a high-output triboelectric nanogenerator material for self-powered anticorrosion *Chem. Eng. J.* **455** 140865

[10] Langer R, Mustonen K, Markevich A, Otyepka M, Susi T and Błoński P 2022 Graphene lattices with embedded transition-metal atoms and tunable magnetic anisotropy energy: implications for spintronic devices *ACS Appl. Nano Mater.* **5** 1562–73

[11] Lin P-C *et al* 2021 Doping graphene with substitutional MN *ACS Nano* **15** 5449–58

[12] Wang J, Gan L, Zhang W, Peng Y, Hong Y, Yan Q, Xia X and Wang X 2018 In situ formation of molecular Ni-Fe active sites on heteroatom-doped graphene as a heterogeneous electrocatalyst toward oxygen evolution *Sci. Adv.* **4** eaa7970

[13] Dehui Deng K S N, Qiang F, Zheng N, Tian Z and Bao X 2016 Catalysis with two-dimensional materials and their heterostructures *Nat. Nanotechnol.* **11** 218–30

[14] Zhang Q and Guan J 2020 Single-atom catalysts for electrocatalytic applications *Adv. Funct. Mater.* **30** 2000768

[15] Cortés-Arriagada D, Villegas-Escobar N and Ortega D E 2018 Fe-doped graphene nanosheet as an adsorption platform of harmful gas molecules (CO, CO_2, SO_2 and H_2S) and the co-adsorption in O_2 environments *Appl. Surf. Sci.* **427** 227–36

[16] Zhou M, Yun-Hao L, Cai Y-Q, Zhang C and Feng Y-P 2011 Adsorption of gas molecules on transition metal embedded graphene: a search for high-performance graphene-based catalysts and gas sensors *Nanotechnology* **22** 385502

[17] Tanaka H *et al* 2002 Electron spin resonance studies of Co(tbp) $C_6$0single crystal *J. Phys.: Condens. Matter* **14** 3993–4000

[18] Konarev D V, Khasanov S S, Saito G, Lyubovskaya R N, Yoshida Y and Otsuka A 2003 The interaction of $C_6$0, $C_7$0 and $C_6$0 $(CN)_2$ radical anions with cobalt(II) tetraphenylporphyrin in solid multicomponent complexes *Chem. Eur. J.* **9** 3837–48

[19] Yoshikawa G, Tsuruma Y, Ikeda S and Saiki K 2009 Noble metal intercalated fullerene fabricated by low temperature Co deposition *Adv. Mater.* **22** 43–46

[20] Vishnoi R, Gupta S, Dwivedi U K and Singhal R 2020 Optical and structural modifications of copper-fullerene nanocomposite thin films by 120 MeV Au ion irradiation *Radiat. Phys. Chem.* **166** 108442

[21] Karczmarska A, Adamek M, Houbbadi S E, Kowalczyk P and Laskowska M 2022 Carbon-supported noble-metal nanoparticles for catalytic applications-a review *Crystals* **12** 584

[22] Joshi G *et al* 2021 Fabrication and applications of fullerene-based metal nanocomposites: a review *J. Mater. Res.* **36** 114–28

[23] Varshney D, Meenu Varshney R K S and Mishra R 1999 Superconductivity in alkali metal doped fullerenes ($K_3C_6$0): a phonon mechanism *J. Phys. Chem. Solids* **60** 579–85

[24] Takeya H, Kato R, Wakahara T, Miyazawa K'ichi, Yamaguchi T, Ozaki T, Okazaki H and Takano Y 2013 Preparation and superconductivity of potassium-doped fullerene nanowhiskers *Mater. Res. Bull.* **48** 343–5

[25] Vacik J, Lavrentiev V, Novotna K, Bacakova L, Lisa V, Vorlicek V and Fajgar R 2010 Fullerene ($C_6$0)-transitional metal (Ti) composites: structural and biological properties of the thin films *Diam. Relat. Mater.* **19** 242–6

[26] Bolokang A S, Phasha M J, Camagu S T, Motaung D E and Bhero S 2012 Effect of thermal treatment on mechanically milled cobalt powder *Int. J. Refract. Met. Hard Mater* **31** 258–62

[27] Kaushik S, Khanderao A G, Pooja Gupta V R R and Kumar D 2022 Growth of ultra-thin cobalt on fullerene ($C_6$0) thin-film: in-situ investigation under UHV conditions *Mater. Sci. Eng. B* **284** 115911

[28] Gupta S, Fernandes R, Patel R, Spreitzer M and Patel N 2023 A review of cobalt-based catalysts for sustainable energy and environmental applications *Appl. Catal. A* **661** 119254

[29] Patel G, Ganss F, Salikhov R, Stienen S, Fallarino L, Ehrler R, Gallardo R A, Hellwig O, Lenz K and Lindner J 2023 Structural and magnetic properties of thin cobalt films with mixed hcp and fcc phases *Phys. Rev. B* **108** 184429

[30] Lee G H, Huh S H, Jeong J W and Ri H-C 2002 Excellent magnetic properties of fullerene encapsulated ferromagnetic nanoclusters *J. Magn. Magn. Mater.* **246** 404–11

[31] Kuznetsov A 2012 Magnetic properties of endohedral complexes $Co_5@C_n$ depending upon the size and symmetry of fullerenes as well as orientation of cobalt cluster *Comput. Mater. Sci.* **54** 204–7

[32] Ceccio G, Vacik J, Lavrentiev V, Tomandl I, Miksova R and Takahashi K 2024 Study of thin film composites based on $LiCoO_2$ and $C_6$0 using neutron depth profiling and atomic force microscopy *J. Radioanal. Nucl. Chem.* **333** 6687–97

[33] Vacik J, Lavrentiev V, Havranek V, Horak P, Hnatowicz V and Fajgar R 2016 Laser-induced periodic surface structure in nickel-fullerene composites *Radiat. Eff. Defects Solids* **171** 154–60

[34] Zalibera M, Ziegs F, Schiemenz S, Dubrovin V, Lubitz W, Savitsky A, Deng S H M, Wang X-B, Avdoshenko S M and Popov A A 2021 Metallofullerene photoswitches driven by photoinduced fullerene-to-metal electron transfer *Chem. Sci.* **12** 7818–38

[35] Vacik J, Lavrentiev V, Hnatowicz V, Vorlicek V and Naramoto H 2009 Hybridization and modification of the Ni/$C_6$0 composites *AIP Conf. Proc.* **1099** 553–6

[36] Sakai S, Naramoto H, Avramov P V, Yaita T, Lavrentiev V, Narumi K, Baba Y and Maeda Y 2007 Comparative study of structures and electrical properties in cobalt–fullerene mixtures by systematic change of cobalt content *Thin Solid Films* **515** 7758–64

[37] Lavrentiev V, Motylenko M, Barchuk M, Schimpf C, Lavrentieva I, Pokorny J, Roder C, Vacik J, Dejneka A and Rafaja D 2020 Structure assembly regularities in vapour-deposited gold–fullerene mixture films *Nanoscale Adv.* **2** 1542–50

[38] Lavrentiev V, Chvostova D, Pokorny J, Lavrentieva I, Vacik J and Dejneka A 2021 Tuneable interplay of plasmonic and molecular excitations in self-assembled silver-fullerene nanocomposites *Carbon* **184** 34–42

[39] Lavrentiev V, Chvostova D, Klementova M, Kuldova K, de Prado E, Vacik J, Lavrentieva I and Dejneka A 2024 Room temperature excitonic coupling in self-assembled copper–Fullerene hybrid films exposed to ambient air *Carbon* **226** 119230

[40] Vacik J, Ceccio G, Lavrentiev V, Miksova R, Havranek V, Pleskunov P and Cannavò A 2024 Study of surface morphology of Ag thin films prepared by sputtering and irradiation with keV Ar ion beam *Radiat. Eff. Defects Solids* **179** 136–45

[41] Mayer M 1999 SIMNRA, a simulation program for the analysis of NRA, RBS and ERDA *AIP Conf. Proc.* **475** 541–4

[42] Klingenberg B, Grellner F, Borgmann D and Wedler G 1993 Oxygen adsorption and oxide formation on Co (1120) *Surf. Sci.* **296** 374–82

[43] Dresselhaus M S, Dresselhaus G and Eklund P C 1996 Raman scattering in fullerenes *J. Raman Spectrosc.* **27** 351–71

[44] Dorner-Reisel A, Ritter U, Moje J, Freiberger E and Scharff P 2022 Effect of fullerene $C_6$0 thermal and tribomechanical loading on Raman signals *Diam. Relat. Mater.* **126** 109036

[45] Ferrari A C and Robertson J 2001 Resonant Raman spectroscopy of disordered, amorphous and diamondlike carbon *Phys. Rev. B* **64** 075414

[46] Martin E J J, Bérubé N, Provencher F, Coté M, Silva C, Doorn S K and Grey J K 2015 Resonance Raman spectroscopy and imaging of push–pull conjugated polymer–fullerene blends *J. Mater. Chem.* **3** 6058–66

[47] Yang Li, Qiu W, Qin F, Fang H, Hadjiev V G, Litvinov D and Bao J 2016 Identification of cobalt oxides with Raman scattering and Fourier transform infrared spectroscopy *J. Phys. Chem. C* **120** 4511–6

[48] Rivas-Murias B and Salgueiriño V 2017 Thermodynamic CoO - Co_3O_4 crossover using Raman spectroscopy in magnetic octahedron-shaped nanocrystals *J. Raman Spectrosc.* **48** 837–41

[49] Available at: https://zenodo.org/uploads/18230442